



## A variational hydraulic fracturing model coupled to a reservoir simulator



Keita Yoshioka <sup>a,\*</sup>, Blaise Bourdin <sup>b</sup>

<sup>a</sup> Chevron Energy Technology Company, 1500 Louisiana St., Houston, TX 77002, USA

<sup>b</sup> Department of Mathematics, Louisiana State University, Baton Rouge, LA 70803, USA

### ARTICLE INFO

#### Article history:

Received 20 November 2015

Received in revised form

16 July 2016

Accepted 25 July 2016

Available online 3 August 2016

#### Keywords:

Hydraulic fracturing

Numerical simulation

Variational approach

Phase field

### ABSTRACT

A variational fracture model coupled to an external reservoir simulator through variable exchange is presented. While convergence is not optimal without Jacobian matrices with which fully coupling can provide, the presented coupling scheme is versatile enough that the reservoir simulator could be easily replaced with any other simulator. A variational approach to fracture is introduced first by comparison to the classic Griffith criteria, and is then expanded to include poro-elasticity and in-situ stresses that are required in hydraulic applications. The coupled code has been tested against existing analytical solutions of fluid-driven fracture propagation. Finally, illustrative examples are shown to demonstrate that the methodology's ability to simulate multi fracture interaction with the unified approach for turning and merging fractures.

© 2016 Elsevier Ltd. All rights reserved.

### 1. Introduction

In predicting fracture propagation during well stimulation or water/waste injection, it is crucial to properly understand the behavior of the fractures induced. For example, the assumption of a single planar fracture propagation often leads to an estimation of an unrealistically long fracture given the volume of injection in water injection operation, which then leads to an over-specification of water treatment program with higher capital and operating expenditure,<sup>1,2</sup> or not accounting for interaction with existing fractures (either man-made or pre-existing) may result in unfavorable well spacing for tight rock development, which can lead to increased number of wells or hydraulic stimulation stages.<sup>3,4,5</sup> Thus the urgency to develop predictive capabilities for complex hydraulic fracture propagation (turning, merging, and branching) is increasing in the industry as well as the requirement for complex flow behaviors such as fluid phase change or particle deposition in porous media.

To date, most hydraulic fracturing simulations have focused upon the problem of a single mode-I fracture on a vertical plane driven by a pressurized fluid applying Linear Elastic Fracture Mechanics (LEFM) as propagation criteria coupled with Poiseuille's equation of fluid flow in the fracture and Carter's equation for leak-off to the formation. A thorough historical background and review of the LEFM based approach on 2D, pseudo 3D, and full 3D

fracture modeling has been conducted by Adachi.<sup>6</sup> Additionally models that consider flow in both reservoir and fracture flow instead of treating fluid leak off with Carter's equation have been proposed.<sup>7,8,9,10</sup> Lujun et al.<sup>7</sup> applied hydraulic force as boundary force on the fracture placed in the boundary. A cohesive element approach on a planar fracture<sup>8</sup> and a turning mix-mode fracture, and sub-grid enrichment of finite element method<sup>10</sup> have been also studied.

For hydraulic fracture models in the presence of natural pre-existing fractures, Kresse et al.<sup>11</sup> utilized pseudo 3D approach for the propagating main fracture and semi-analytical crossing criteria for interaction with pre-existing natural fractures. Natural fractures were treated as closed weak planes and its mechanical interaction with hydraulic fractures was computed with a 2D Boundary Element Method (BEM) by incorporating empirically derived 3D effects. McClure et al.<sup>12</sup> applied the LEFM approach for the criteria for hydraulic fracture initiation and propagation on the prescribed plane using fixed grid for growth of fracture and utilized BEM for stress disturbance by natural fracture opening and shearing. Similarly to Kresse et al.<sup>11</sup>, semi-analytical crossing criteria proposed by Gu and Weng<sup>13</sup> were used for interaction between hydraulic fractures and natural fractures. A Discrete Element Method (DEM) has been also applied to hydraulic fracturing with natural fractures.<sup>14</sup> In the DEM framework, hydraulic fractures propagate along prescribed element boundaries when a stress intensity factor meets the criteria, and the natural fracture opening is estimated using a Coulomb friction model. While the stress shadow effects of opening fractures were accounted in these studies, poroelastic impacts induced by leak-off were not included.

\* Corresponding author.

E-mail address: [yoshk@chevron.com](mailto:yoshk@chevron.com) (K. Yoshioka).

Recently, simulation approaches to complex fracture(s) along unknown path(s) have been developed using different techniques such as a BEM or an extended finite element method (XFEM). Wu and Olson<sup>15</sup> modeled 2D fractures that propagate in both mode-I and II using 3D correction in the BEM formulation. Complex single fracture propagation in 3D has been developed by Rungamornrat and Mear.<sup>16</sup> Their model has been extended to multiple fracture propagation and interaction by Castonguay et al.<sup>17</sup> An XFEM has been first applied to hydraulic fracture by incorporating pressure forces along a line fracture in 2D impermeable media by Lecampion<sup>18</sup> for stationary fracture. Dahi-Taleghani and Olson<sup>19</sup> implemented the XFEM for propagating fracture in 2D and Gordeljiy and Peirce<sup>20</sup> extended the methodology to include solid-fluid interaction at the fracture tip. While these methods are appealing for not requiring a priori knowledge of the crack path, the BEM imposes restrictions on heterogeneity in material properties and handling of merging fractures remains as a perplexing challenge.

The variational approach to fracture was originally proposed by Francfort and Marigo<sup>21</sup> and was numerically implemented by Bourdin et al.<sup>22,23</sup> using a “phase-field” approach. This approach is capable of tracking arbitrary number of fractures in any geometry, regardless of the propagation mode. It was extended to hydraulic fracturing in impermeable media by accounting for the work of the pressure forces applied along the fracture in Bourdin et al.,<sup>24</sup> where it was shown that explicit properties such as fracture aperture or critical propagation pressure could be retrieved from the phase field. Phase-field’s implicit representation of the fracture system has proved useful in hydraulic fracturing simulations and its initial application has been followed by many others.<sup>25,26,27,28,29,30</sup> Wheeler et al.<sup>25</sup> extended the phase-field model to porous media by including poroelastic terms in the total energy. Its implementation has been enhanced with adaptive finite element in 2D<sup>27</sup> and 3D.<sup>29</sup> Wick et al.<sup>30</sup> coupled the methodology to a reservoir simulator using an indicator function for fractures. Miehe et al.<sup>28</sup> coupled porous media flow with the phase-field hydraulic fracture using permeability decomposition and the unilateral contact condition.<sup>31</sup> Mikelic et al.<sup>26</sup> fully coupled the three-field problems and modified the total energy functional from their previous studies.

In this article, we show how a phase-field fracture model of fracture and an existing reservoir simulator can be coupled with minimal modifications. The main motivation for this approach, over that seeking to leverage the phase-field description of the fracture in the flow model,<sup>32,33</sup> is that it allows reusing a feature-rich, validated reservoir simulator. The proposed coupling is iterative, and does not allow sharing information on the Jacobians. However, it uses the same computational grid for the mechanics and flow solvers, so that constructing an explicit mesh of the fracture geometry is not required, and is reasonably efficient. In the sequel, we describe the construction of the phase field model, the implementation of the coupled simulator, and illustrate the ability of the this approach to handle critical features such as crack propagation along unknown path in two and three dimension, ability to handle interactions between stimulated and pre-existing fractures, and nucleation of new add-cracks.

## 2. Mathematical model

### 2.1. Variational approach to fracture

Consider a domain  $\Omega$  in 2 or 3D, occupied by a brittle linearly elastic material with stiffness tensor  $\mathbf{C}$ , and a fracture set  $\Gamma$  and critical energy release rate (fracture toughness)  $G_c$  (Fig. 1a). Let  $\mathbf{f}(t, x)$  denote a time-dependent body force applied to  $\Omega$ ,  $\tau(t, x)$  a

surface force applied to a part  $\partial_N\Omega$  of its boundary whose normal vector is  $\mathbf{n}_\Omega$ , and  $\mathbf{g}(t, x)$  a prescribed boundary displacement on the remaining part  $\partial_D\Omega$ .

The stress-strain relationship is given as

$$\boldsymbol{\sigma} = \mathbf{C}e(\mathbf{u}) \quad (1)$$

where  $\boldsymbol{\sigma}$  is the stress field, and  $e(\mathbf{u}) = \frac{1}{2}(\nabla\mathbf{u} + \nabla^T\mathbf{u})$  is the strain field, and the equilibrium equations in strong form are:

$$-\nabla \cdot \boldsymbol{\sigma} = \mathbf{f} \text{ in } \Omega/\Gamma, \quad (2)$$

$$\boldsymbol{\sigma} \cdot \mathbf{n}_\Omega = \boldsymbol{\tau} \text{ on } \partial_N\Omega, \quad (3)$$

$$\mathbf{u} = \mathbf{g} \text{ on } \partial_D\Omega. \quad (4)$$

No stress and positive or zero displacement discontinuity on the fracture surface are assumed:

$$\boldsymbol{\sigma} \cdot \mathbf{n} = 0 \text{ on } \Gamma, \quad (5)$$

$$(\mathbf{u}^+ - \mathbf{u}^-) \cdot \mathbf{n} \geq 0 \text{ on } \Gamma. \quad (6)$$

where  $\mathbf{u}^+$  and  $\mathbf{u}^-$  are the displacement on each surface of the fracture. The total external work  $W$  consists of the work by the body force and the external load and is defined for any kinematically admissible displacement  $\mathbf{u}$  as

$$W(\mathbf{u}) := \int_{\Omega} \mathbf{f} \cdot \mathbf{u} d\Omega + \int_{\partial_N\Omega} \boldsymbol{\tau} \cdot \mathbf{u} ds. \quad (7)$$

The potential energy  $E$  is given by the elastic energy of the system subtracting the external work as:

$$E(\mathbf{u}, \Gamma) := \int_{\Omega/\Gamma} e(\mathbf{u}) : \mathbf{C}e(\mathbf{u}) d\Omega - W(\mathbf{u}). \quad (8)$$

The variational approach to fracture proposed by Francfort and Marigo<sup>21</sup> defines the total energy as the sum of the potential energy and the surface energy required to create a fracture set  $\Gamma$ :

$$F(\mathbf{u}, \Gamma) = E(\mathbf{u}, \Gamma) + G_c H^{N-1}(\Gamma), \quad (9)$$

where  $H$  is the Hausdorff measure of  $\Gamma$  providing the fracture length in 2D ( $N = 2$ ) and the surface area in 3D ( $N = 3$ ).

In the Griffith theory, a single fracture in 2D with the length  $l$  is considered and the elastic energy release rate  $G$  can be calculated along an a priori known fracture path as:

$$G = \frac{dE}{dl}. \quad (10)$$

The criteria state that the fracture will propagate when  $G = G_c$  and not when  $G < G_c$ , which is nothing but the criticality of the total energy of the system:

$$F(\mathbf{u}, l) = E(\mathbf{u}, \Gamma) + G_c l. \quad (11)$$

In the variational setting, the Griffith criteria are recast as the minimum of the total energy (Eq. (9)) with respect to any admissible displacement field  $\mathbf{u}$  and any fracture set subject to an irreversibility condition. Namely, at any time step  $t_i$ ,  $(\mathbf{u}_i, \Gamma_i)$  is sought as the solution of the minimization problem:

$$\inf_{\left\{ \begin{array}{l} \mathbf{u} \text{ kinematically admissible} \\ \Gamma_j \subset \Gamma \text{ for all } j < i \end{array} \right.} F(\mathbf{u}, \Gamma) \quad (12)$$

It should be emphasized that in Eq. (12) no assumption on the geometry of the fracture is made a priori. Therefore, fractures are allowed to take an arbitrary path (turning or bifurcating), and the number of fracture does not need to remain constant, which

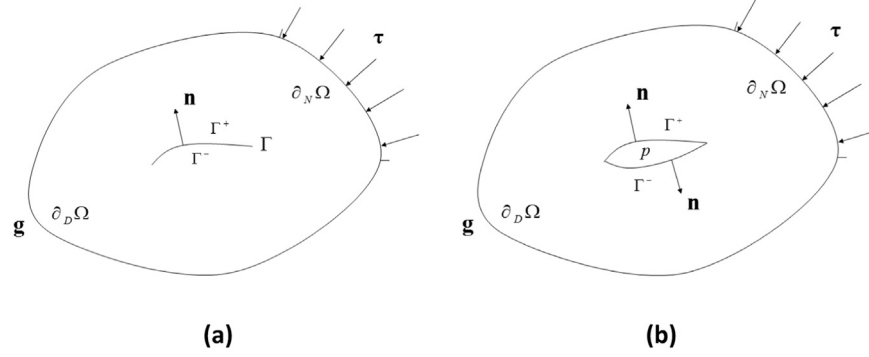


Fig. 1. Schematic of the problem setting for fracturing in: (a) elastic medium and (b) porous medium.

allows nucleation and merging of fractures. The numerical implementation of Eq. (12) is challenging as it involves discontinuities (fracture set) and the discontinuities are not known a priori. Bourdin et al.<sup>22</sup> proposed an approach based on the variational approximation by elliptic functional.<sup>34,35</sup> A regularization parameter  $\varepsilon$  is introduced and the fracture is represented a smooth phase field function  $v$  approaching values 0 close to the fracture and 1 far from them. The total energy can be expressed using  $\varepsilon$  and  $v$  as:

$$F_\varepsilon(\mathbf{u}, v) = \int_\Omega v^2 e(\mathbf{u}) : \mathbf{C}e(\mathbf{u}) d\Omega - \int_\Omega \mathbf{f} \cdot \mathbf{u} d\Omega + \int_{\partial_N \Omega} \boldsymbol{\tau} \cdot \mathbf{u} ds + \frac{3G_c}{8} \int_\Omega \frac{(1-v)}{\varepsilon} + \varepsilon |\nabla v|^2 d\Omega. \quad (13)$$

It can be shown that the regularized total energy  $F_\varepsilon$  approaches to  $F$  as  $\varepsilon$  approaches to 0 in the sense of  $\Gamma$ -convergence, meaning that the minimizers of  $F_\varepsilon$  converge to those of  $F$ . From a numerical standpoint, the main feature of the regularized energy representation is that the fracture set does not require explicit treatment as discontinuous field, and computations can be carried out on a fixed mesh to represent complex fracture path using the phase field function.

## 2.2. Extension to hydraulic fracture in porous media

In hydraulic fracturing, propagation is induced by the increase of fluid pressure in the fractures or through the perforations (Fig. 1b). Bourdin et al.<sup>24</sup> adapted the variational approach to hydraulic fracturing by accounting for fluid pressure forces along the fracture surfaces. The previous model can be further extended to porous media. The stress-strain relationship is given as:

$$\boldsymbol{\sigma} = \mathbf{C}e(\mathbf{u}) - \alpha p \mathbf{I}, \quad (14)$$

$$= \boldsymbol{\sigma}^e - \alpha p \mathbf{I}.$$

where  $\boldsymbol{\sigma}^e$  is the effective stress, and  $\alpha$  and  $p$  are the Biot's coefficient and the pore-pressure respectively. The equilibrium equation is similarly:

$$-\nabla \cdot \boldsymbol{\sigma} = \mathbf{f} \quad \text{in } \Omega \setminus \Gamma. \quad (15)$$

On the fracture surface, force balance and positive or zero displacement discontinuity on the fracture surface (no interpenetration) are assumed

$$\boldsymbol{\sigma} \cdot \mathbf{n} = -p \mathbf{n} \quad \text{on } \Gamma, \quad (16)$$

$$(\mathbf{u}^+ - \mathbf{u}^-) \cdot \mathbf{n} \geq 0 \quad \text{on } \Gamma. \quad (17)$$

In order to derive the elastic energy for porous media, consider a virtual displacement  $\tilde{\mathbf{u}} \in H^1(\Omega/\Gamma)$  such that  $\tilde{\mathbf{u}} = 0$  on  $\partial_D \Omega$ .

Multiplying both sides of the equilibrium equation, over  $\Omega/\Gamma$  yields,

$$-\int_{\Omega/\Gamma} \nabla \cdot \boldsymbol{\sigma} \cdot \tilde{\mathbf{u}} d\Omega = \int_{\Omega/\Gamma} \mathbf{f} \cdot \tilde{\mathbf{u}} d\Omega. \quad (18)$$

Integrating by parts and applying divergence theorem give

$$\int_{\Omega/\Gamma} \boldsymbol{\sigma} : e(\tilde{\mathbf{u}}) d\Omega - \int_{\partial_N \Omega} \boldsymbol{\sigma} \cdot \mathbf{n} \cdot \tilde{\mathbf{u}} dS - \int_\Gamma \boldsymbol{\sigma} \cdot \mathbf{n} \cdot [\tilde{\mathbf{u}}] dS = \int_{\Omega/\Gamma} \mathbf{f} \cdot \tilde{\mathbf{u}} d\Omega. \quad (19)$$

Substituting Eqs. (16) and (17) into Eq. (19) yields,

$$\int_{\Omega/\Gamma} \boldsymbol{\sigma} : e(\tilde{\mathbf{u}}) d\Omega - \int_{\partial_N \Omega} \boldsymbol{\tau} \cdot \tilde{\mathbf{u}} dS + \int_\Gamma p \mathbf{n} \cdot [\tilde{\mathbf{u}}] dS = \int_{\Omega/\Gamma} \mathbf{f} \cdot \tilde{\mathbf{u}} d\Omega \quad (20)$$

Substituting the stress-strain relationship (Eq. (14)) into Eq. (20) yields,

$$\begin{aligned} & \int_{\Omega/\Gamma} (\mathbf{C}e(\mathbf{u}) - \alpha p \mathbf{I}) : e(\tilde{\mathbf{u}}) d\Omega - \int_{\partial_N \Omega} \boldsymbol{\tau} \cdot \tilde{\mathbf{u}} dS + \int_\Gamma p \mathbf{n} \cdot [\tilde{\mathbf{u}}] dS \\ & - \int_{\Omega/\Gamma} \mathbf{f} \cdot \tilde{\mathbf{u}} d\Omega. \\ & = \int_{\Omega/\Gamma} \mathbf{C}e(\mathbf{u}) : e(\tilde{\mathbf{u}}) d\Omega - \int_{\Omega/\Gamma} \alpha p \mathbf{I} : e(\tilde{\mathbf{u}}) d\Omega - \int_{\partial_N \Omega} \boldsymbol{\tau} \cdot \tilde{\mathbf{u}} dS \\ & + \int_\Gamma p \mathbf{n} \cdot [\tilde{\mathbf{u}}] dS - \int_{\Omega/\Gamma} \mathbf{f} \cdot \tilde{\mathbf{u}} d\Omega = 0 \end{aligned} \quad (21)$$

In order for Eq. (21) to be the first order optimality, the elastic energy functional needs to be

$$E(\mathbf{u}) = - \int_{\partial_N \Omega} \boldsymbol{\tau} \cdot \mathbf{u} dS + \int_\Gamma p \mathbf{n} \cdot [\mathbf{u}] dS - \int_{\Omega/\Gamma} \mathbf{f} \cdot \mathbf{u} d\Omega. + \frac{1}{2} \int_{\Omega/\Gamma} \mathbf{C} \left( e(\mathbf{u}) - \frac{\alpha}{3\kappa} p \mathbf{I} \right) : \left( e(\mathbf{u}) - \frac{\alpha}{3\kappa} p \mathbf{I} \right) d\Omega. \quad (22)$$

Following Bourdin et al.<sup>24</sup>, the fracture volume can be recovered using the gradient of the phase field damage as:

$$\int_\Gamma (\mathbf{u}^+ - \mathbf{u}^-) \cdot \mathbf{n} dS = \int_{\Gamma^+} \mathbf{n} \cdot \mathbf{u}^+ dS - \int_{\Gamma^-} \mathbf{n} \cdot \mathbf{u}^- dS \approx - \int_\Omega \mathbf{u} \cdot \nabla v d\Omega. \quad (23)$$

The regularized total energy for a poroelastic medium can be defined as:

$$F_\varepsilon(\mathbf{u}, v) = \frac{1}{2} \int_\Omega \mathbf{C} \left( ve(\mathbf{u}) - \frac{\alpha}{3\kappa} p \mathbf{I} \right) : \left( ve(\mathbf{u}) - \frac{\alpha}{3\kappa} p \mathbf{I} \right) d\Omega + \frac{3G_c}{8} \int_\Omega \frac{1-v}{\varepsilon} + \varepsilon |\nabla v|^2 d\Omega - \int_{\partial_N \Omega} \boldsymbol{\tau} \cdot \mathbf{u} dS - \int_\Gamma p \mathbf{u} \cdot \nabla v d\Omega - \int_{\Omega/\Gamma} \mathbf{f} \cdot \mathbf{u} d\Omega. \quad (24)$$

## 2.3. Unilateral contact condition

The total energy given in Eq. (24) is symmetric in tension and compression, which means compressive fracture with negative fracture volume is as admissible as tensile fracture with positive

fracture volume given a displacement field depending on the direction of the load. This becomes clearer when fracture(s) pre-exist under in-situ stresses, which is discussed in one of the examples later. Amongst all the methods that have been proposed to deal with this unilateral contact along fractures,<sup>31,36,37</sup> we chose that of Amore et al.<sup>38</sup> in parts for the simplicity and efficiency of its implementation, and because it is theoretically better understood.<sup>37</sup> In this approach, the elastic strain  $e(\mathbf{u})$  is decomposed in its spherical and deviatoric components as:

$$e(\mathbf{u}) = e_S(\mathbf{u}) + e_D(\mathbf{u}), \quad (25)$$

where

$$e_S(\mathbf{u}) = \frac{1}{N} \text{tr}(e(\mathbf{u})) \mathbf{I}, \quad (26)$$

$$e_D(\mathbf{u}) = e(\mathbf{u}) - \frac{1}{N} \text{tr}(e(\mathbf{u})) \mathbf{I}. \quad (27)$$

and  $N$  is space the dimension ( $N = 2$  for 2D and  $N = 3$  for 3D). Using this decomposition, the elastic energy density  $\mathbf{C}: e(\mathbf{u}): e(\mathbf{u})$  can be written as

$$\mathbf{C}e(\mathbf{u}): e(\mathbf{u}) = \kappa_0 \frac{\text{tr}(e(\mathbf{u}))^2}{2} + \mu e_D(\mathbf{u}): e_D(\mathbf{u}), \quad (28)$$

where  $\kappa_0$  and  $\mu$  are the bulk and shear modulus respectively. In order to prevent material interpenetration along cracks, the elastic energy density is modified to distinguish contributions from the compressive (the negative volume change) and the tensile regions (the positive volume change). The elastic energy density can be decomposed into:

$$\mathbf{C}e(\mathbf{u}): e(\mathbf{u}) = \kappa_0 \frac{\text{tr}^+(e(\mathbf{u}))^2}{2} + \kappa_0 \frac{\text{tr}^-(e(\mathbf{u}))^2}{2} + \mu e_D(\mathbf{u}): e_D(\mathbf{u}), \quad (29)$$

where  $\text{tr}^+(e(\mathbf{u})) = \max[\text{tr}(e(\mathbf{u})), 0]$  and  $\text{tr}^-(e(\mathbf{u})) = \max[-\text{tr}(e(\mathbf{u})), 0]$ . Combining Eqs. (24) and (29), we obtain the total mechanical energy:

$$\begin{aligned} F_e(\mathbf{u}, v) = & \frac{1}{2} \int_{\Omega} \kappa_0 \text{tr}^+ \left( v e(\mathbf{u}) - \frac{\alpha}{3\kappa} p \mathbf{I} \right)^2 + \kappa_0 \text{tr}^- \left( e(\mathbf{u}) - \frac{\alpha}{3\kappa} p \mathbf{I} \right)^2 \\ & + \mu v^2 e_D(\mathbf{u}): e_D(\mathbf{u}) d\Omega + \frac{3C_c}{8} \int_{\Omega} \frac{1-v}{\varepsilon} + \varepsilon |\nabla v|^2 d\Omega \\ & - \int_{\partial_N \Omega} \boldsymbol{\tau} \cdot \mathbf{u} dS - \int_{\Omega} p \mathbf{u} \cdot \nabla v d\Omega - \int_{\Omega} \mathbf{f} \cdot \mathbf{u} d\Omega \end{aligned} \quad (30)$$

and the energy minimization problem (Eq. (12)) becomes at any given time step  $i$

$$\inf_{\left\{ \begin{array}{l} \mathbf{u} \text{ kinematically admissible} \\ 0 \leq v \leq v_{i-1} \leq 1 \end{array} \right.} F_e(\mathbf{u}, v) \quad (31)$$

#### 2.4. Numerical implementation of variational hydraulic-fracture

Coupling with a reservoir simulator is achieved through variable exchanges at each time step. From the reservoir simulator, a pore-pressure field is provided to the variational hydraulic-fracture simulator, which seeks the minimization of the total energy functional (Eq. (30)). Given the pressure field, the variational hydraulic-fracture simulator solves for  $\mathbf{u}$  and  $v$  and then sends multipliers of the permeability to the reservoir simulator. We follow the approach of Bourdin et al.<sup>22,23</sup> At any given time step  $i$ , alternate minimization with respect to  $\mathbf{u}$  given  $v$  and  $p$ , constrained minimization with respect to  $v$ , given  $\mathbf{u}$  and  $p$ , and computation of the pressure  $p$  are performed. This process is repeated until  $p$  until the convergence

criteria  $\|v^l - v^{l-1}\| < \delta_v$  and  $\|p^l - p^{l-1}\| < \delta_p$ , where  $\delta_v$  and  $\delta_p$  are the tolerance for  $v$  and  $p$  respectively are met.

In our implementation,  $\mathbf{u}$  and  $v$  are discretized using bilinear quadrilateral finite elements. The minimization of the total energy with respect to  $\mathbf{u}$  is achieved through a Newton algorithm and that with respect to  $v$  is formulated as a variational inequality problem. Both parallel solvers are provided by PETSc.<sup>39,40</sup>

Accounting for the fracture system in the reservoir simulator is achieved through permeability multipliers. For the sake of simplicity, consider a porous medium with porosity  $\varphi$  occupied by a single-phase fluid with density  $\rho$ , a reservoir simulator solves a mass balance:

$$\frac{\partial}{\partial t}(\varphi \rho) = -\nabla \cdot (\rho \mathbf{U}) + q \quad (32)$$

where  $q$  is the source term and the fluid velocity  $\mathbf{U}$  is given by

$$\mathbf{U} = -\frac{k_{mult} \mathbf{K}}{\mu} \cdot (\nabla p - \gamma \nabla D), \quad (33)$$

where  $k_{mult}$  is the permeability multiplier,  $\mathbf{K}$  is the permeability tensor,  $\mu$  is the viscosity,  $\gamma$  is the density gradient, and  $D$  is the depth. The permeability multiplier is a scalar value and can be computed as a function of both  $\mathbf{u}$  and  $v$ . For this study, it is simply associated with  $v$  using a step function,

$$k_{mult} = \begin{cases} k_f/k_m, & \text{for } v < v_{th} \\ 1, & \text{otherwise} \end{cases} \quad (34)$$

where  $k_f$  and  $k_m$  are the permeability of fracture and matrix respectively, and  $v_{th}$  is a threshold value for  $v$ .

In the numerical simulations below, we used an in-house reservoir simulator, and the permeability multipliers are updated at each iteration of the reservoir simulator's Newton algorithm. This requires only minimal changes to the reservoir simulator: after each iteration of the Newton solver, the pressure is sent to the phase-field fracture code, and the permeability multipliers are received. Additionally, the convergence criteria were altered in order to communicate to the reservoir simulator that mechanical equilibrium has been achieved. The algorithm used to solve the three-field ( $\mathbf{u}, v$ , and  $p$ ) for is shown in Algorithm 1.

**Algorithm 1.** : Three-field problem.

Set  $p^0, \mathbf{u}^0 = 0, v^0 = 1, t^0 = 0, i = 0$

**Repeat**

$i \leftarrow i + 1, t^i \leftarrow t^{i-1}, j = 0$

$p^j \leftarrow p^{j-1}$

$v^j \leftarrow v^{j-1}$

$\mathbf{u}^j \leftarrow \mathbf{u}^{j-1}$

**Repeat**

$j \leftarrow j + 1$

Compute  $\mathbf{u}^j$  by minimizing (Eq. (30)) with respect to  $\mathbf{u}$  given  $p_{j-1}^i$  and  $v_{j-1}^i$ .

Compute  $v^j$  by minimizing (Eq. (30)) with respect to  $v$  given  $p_{j-1}^i$  and  $\mathbf{u}^j$ .

Compute  $k_{mult,j}^i$  using (Eq. (34)).

Update  $p_j^i$  from  $p_{j-1}^i$  by running a single Newton iteration of the reservoir simulator.

**Until**  $\|v^l - v^{l-1}\| < \delta_v$  and  $\|p^l - p^{l-1}\| < \delta_p$  in addition to other reservoir simulator criteria.

**Until**  $t^i = T$ .

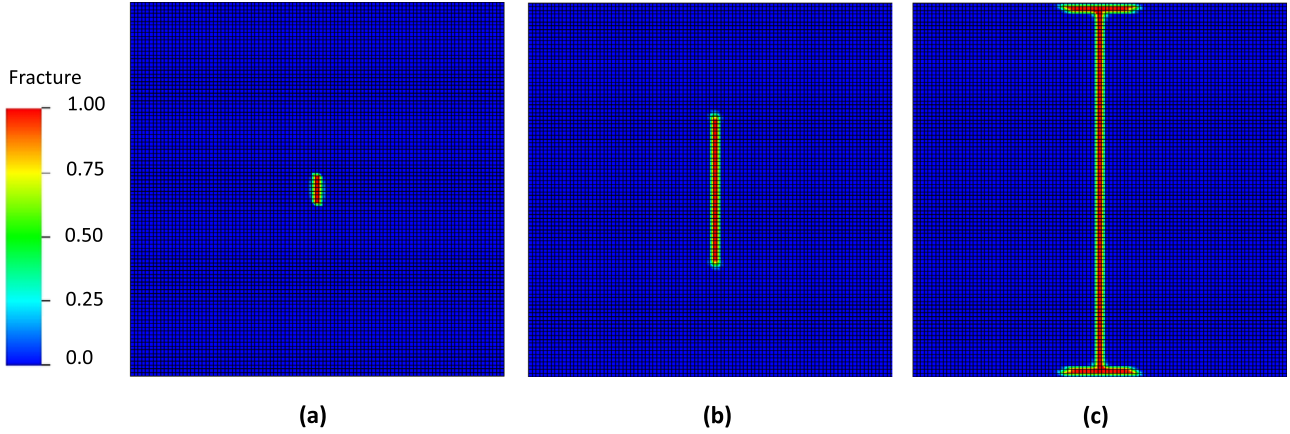


**Fig. 2.** (a) Example computation domain for 2D. A phase field function profile is shown where 0 (blue color) represents fracture and 1 (red color) for intact rock. The domain is discretized with  $100 \times 100 \times 1$  elements. (b) Propagated fracture represented by the phase field function at injected volume of 5.6 bbl. (c) Fracture propagation after 46.4 bbl of injection.

### 3. Numerical testing of the coupled model

Since the coupling between the fluid flow and fracture propagation in this study is achieved through an approximated permeability function rather than cubic law, exact comparison of fracture propagation behavior is not viable with existing closed form solution where the fracture permeability is considered infinite<sup>41</sup> or a function of fracture width using Reynold's lubrication theory.<sup>42–46</sup> Therefore, the coupled model is only “tested” against the theoretical critical pressure at the onset of fracture propagation. As the implementation is done in 3D, all 2D examples in the followings are run with a single layer 3D domain.

For a 2D test in plane stress state, a single pre-existing fracture with length  $2l_0$  in the  $x = 0$  plane in an infinite elastic media is considered. For the internally pressurized fracture, the opening for  $-l_0 \leq y \leq l_0$  is given by Sneddon and Lowengrub<sup>41</sup> as

$$u^+(0, y) = \frac{2pl_0}{E'} \left( 1 - \frac{y^2}{l_0^2} \right)^{1/2} \quad (35)$$

where  $E'$  is the plane strain Young's modulus and  $E' = E/(1 - \nu^2)$ . Since  $u^+(0, y) = u^-(0, y)$ , the fracture volume is  $V = 2\pi l_0^2/E'$  and the strain energy  $E_b$  is

$$E_b = -\frac{1}{2}pV = -\frac{\pi l_0^2 p^2}{E'} \quad (36)$$

Given the fracture toughness  $G_c$ , the propagation pressure  $p_c$  can be obtained from the Griffith's criteria ( $-\partial E_b/\partial 2l_0 = G_c$ ). Therefore, the critical pressure for fracture propagation is

$$p_c = \left( \frac{E'G_c}{\pi l_0} \right)^{1/2} \quad (37)$$

In 3D, a penny-shape fracture with the radius  $r_0$  embedded in an infinite elastic media is considered. Similarly, the displacement field for the internally pressurized fracture from<sup>41</sup> is:

$$u^+(r, 0) = \frac{4pr_0}{\pi E'} \left[ 1 - \left( \frac{r}{r_0} \right)^2 \right]^{1/2} \quad (38)$$

where  $r = \sqrt{x^2 + y^2}$ . Thus the fracture volume is  $V = \int_{\Omega} (u^+ - u^-) dr = 16\pi r_0^3 p / 3E'$  and the strain energy is similarly

$$E_b = -\frac{8r_0^3 p^2}{3E'} \quad (39)$$

The criticality of the strain energy is again given at  $-\partial E_b/\partial A = G_c$  where  $A$  is the area of the fracture,  $A = \pi r_0^2$ . Therefore, the propagation pressure for the penny-shape fracture is

$$p_c = \left( \frac{E'G_c\pi}{4r_0} \right)^{1/2} \quad (40)$$

When in-situ stresses are considered, the propagation pressure for a fracture orthogonal to the minimum stress is given as

$$p_{\text{propagation}} = \sigma_{\min} + p_c \quad (41)$$

In the following examples, various cases of in-situ stress (isotropic) were tested. All the computations were performed with single phase (water), and no thermal effects were included. In all the computations, a rock formation with the fracture toughness of 40 psi-ft, the Young's modulus of 1e6 psi, the poisson's ratio of 0.0, the Biot's coefficient of 1.0, the pore-pressure of 8000 psi, the porosity of 0.1, and the matrix permeability of 0.01 md is considered. The permeability multiplier (Eq. (34)) is set at 1e4.

For 2D examples, we considered a domain of 800 ft by 800 ft with a pre-existing fracture with length of 48 ft in the middle (Fig. 2a). Injection is a line source along the pre-existing fracture with the injection rate of 50 bpm. Fig. 2a shows the profile of the phase field variable  $v$ , where  $v = 0$  (red) represents fracture and  $v = 1$  (blue) for intact rock. As the fracture is pressurized and the pressure reaches the critical propagation pressure, the fracture propagation takes place. Fig. 2b shows a propagated fracture after 5.6 bbl of injection with the in-situ stresses of 8300 psi. As can be seen in Fig. 2b, the propagation of the fracture is traced by the phase field function. The pressure field at the same time step is shown in Fig. 3. Despite the tight permeability of the formation (0.01 md), leak-off of fluids to the formation still can be observed and the pressure field depicts an elliptic profile as the more fluid leaks off closer to the injection well.

For 3D examples, a domain of 800 ft  $\times$  800 ft  $\times$  800 ft and discretization of  $50 \times 50 \times 50$  with a horizontal penny-shape fracture with radius of 20 ft in the center is considered. The initial profile of fracture field ( $v$ ) in the  $xy$  plane ( $z = 400$  ft) is shown in Fig. 4a. An injection source is placed in the center of the penny-shape fracture at the rate of 50 bpm, and the in-situ stresses are isotropic at 8300 psi. As the size of element is 16 ft while the initial radius of fracture is 20 ft, the element resolution may look too coarse to capture fracture propagation. Our previous study in impermeable rock formations<sup>24</sup> shows that the fracture volume can be retrieved from the phase field variable and that it approaches to the theoretical value as the element size decreases. The fracture

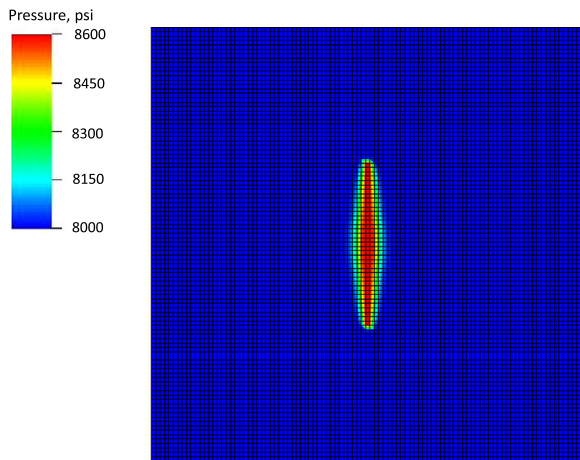


Fig. 3. Pressure profile at injected volume of 5.6 bbl.

Table 1  
Fracture propagation pressure comparison.

2D		
In-Situ stress [psi]	Theory [psi]	Simulation [psi]
8300	9192	9214
8500	9392	9594
8700	9592	9958
9000	9892	10,474
3D		
In-Situ stress [psi]	Theory [psi]	Simulation [psi]
8300	9834	10,416
8500	10,034	11,138
8700	10,234	11,868
9000	10,534	12,842

the test results are reasonably close to the closed form solutions.

Lastly from the test example case, a late stage of the 2D fracture propagation case is shown in Fig. 2c to highlight one of the unique capabilities of the methodology. It can be seen that the line fracture reached to the domain boundaries, branched, and then continued to propagate along the domain boundaries. This propagation itself is affected by the domain boundary and the fracture was not given a choice to grow straight. However, it demonstrates the methodology's capability to simulate branching fracture and also implies what might happen to a fracture at layer boundaries with significant mechanical property difference (e.g. sand-shale). This pattern of fracture propagation is also known as "T-shape fracture".

propagation after 7835 bbl of injection is shown in Fig. 4b. Despite the coarse initial "penny-shape" due to the element resolution, the fracture propagated symmetrically on the initial xy plane in 3D space and maintained a clean penny shape.

In both the 2D and 3D examples, various in-situ stress cases were imposed and the simulated fracture propagation pressures are compared against the theoretical ones in Table 1. The higher the in-situ stress, the higher pressure is required to propagate the fracture which leads to more leak-off to the formation and a greater pressure gradient within the fracture. However, the closed form solution is based on the assumptions of no-leak off to the formation and constant pressure inside the fracture. Therefore, the deviation from the theoretical value becomes larger when in-situ stresses are higher. Furthermore, leak-off fluids will pressurize the formation and subsequently increase the total stresses in the formation from the in-situ condition. Thus, a higher pressure is required to propagate the fracture than the solutions that do not consider the poro-elastic effects. Nevertheless, despite the simplistic approximation of permeability multiplier as a function of  $v$ ,

#### 4. Interaction with natural (pre-existing) fractures

In this section, we demonstrate the methodology's capabilities of simulating hydraulic fracturing with the presence of natural (pre-existing) fractures under in-situ stresses. We will show computation of hydraulic fracturing interaction with pre-existing natural fractures both in 2D and 3D settings.

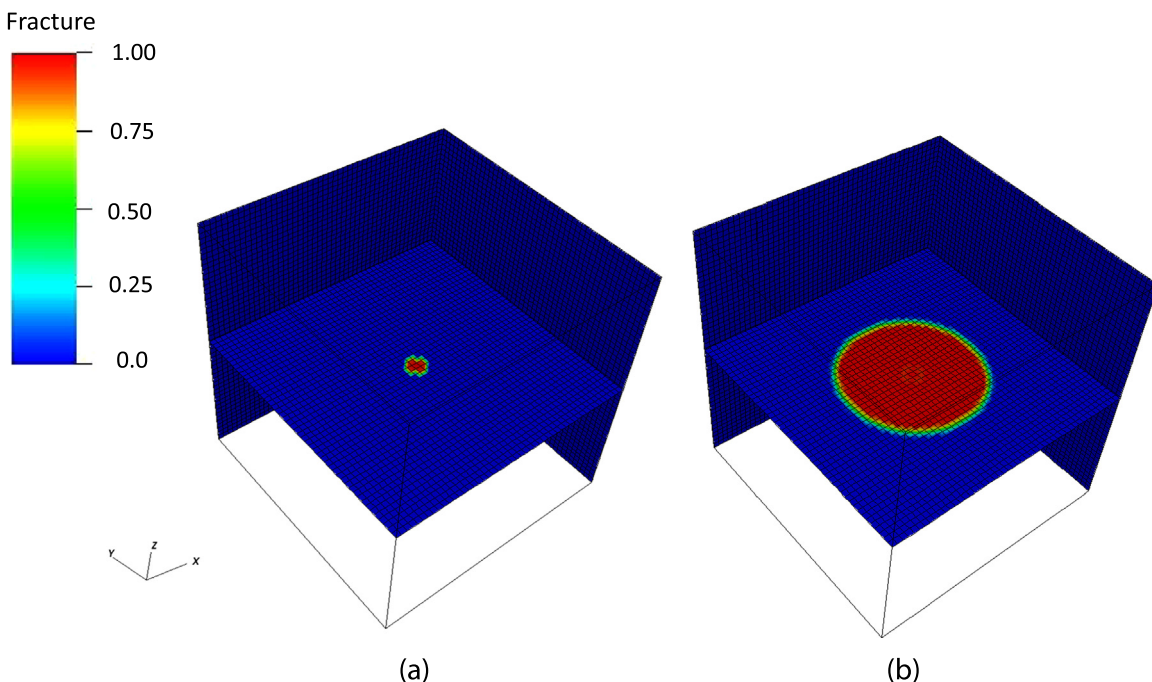


Fig. 4. (a) Example computation domain for 3D. A phase field function profile for an initial horizontal penny-shape fracture is shown on  $z=400$  ft. The domain is discretized with  $50 \times 50 \times 50$  elements. (b) Fracture propagation in 3D test example after 7835 bbl of injection.

#### 4.1. 2D example

Since hydraulic fracturing is conducted in a subsurface environment where in-situ stresses are imposed, almost all pre-existing fractures principally experience compressive stresses. Thus, treatment of pre-existing fracture interpenetration plays a significant role in the simulation of hydraulic fracturing. Before we study hydraulic fracturing interaction with pre-existing fractures in details, we will firstly show the impacts of the unilateral contact condition using a 2D example. Fig. 5 shows a first example with a line oblique fracture located 200 ft away from the injection source in 2D. All the properties are the same as the 2D examples in the previous section except that anisotropic in-situ stress condition is considered (stresses in x- and y-direction are 8500 psi and 8700 psi respectively). Also, note that the same structured regular quadratic mesh is used in these examples. With the phase field methodology, fractures not aligned with the mesh can be easily represented by assigning proper phase field values to each of the node without a need of re-gridding. Similarly to the previous section, water is injected at 50 bpm from the middle fracture as shown in Fig. 5. In all the test examples with a single fracture, the mode of the fracture propagation is mode-I (tensile) forced by elevated pore-pressure. Therefore, the unilateral contact condition in the regularized energy formation is not crucial. However, we will demonstrate its significance with the presence of natural fractures.

Firstly, a simulation was conducted without the unilateral contact condition. The initial displacement fields are shown in Fig. 6. From the initial displacement field, interpenetration of the pre-existing fractures can be observed. Whereas this issue is mitigated immediately after the start of injection in the center fracture as it is pressurized, this is not the case for the oblique pre-existing fracture where the hydraulic support from the fluid, i.e. the pore-pressure inside the fracture is smaller than the surrounding compressive normal stresses. The evolution of the fracture propagation is shown in Fig. 7. It can be observed in Fig. 7 that the hydraulic fracture first propagates away from the pre-existing fracture (Fig. 7a) and turns to “avoid” the pre-existing fracture (Fig. 7b). The reason for this avoidance is actually encouraged by the initial displacement field imposed by the interpenetration at the oblique fracture. Since the vicinity formation is sucked into the oblique pre-existing fracture, part of the rock is “stretched” and creates a preferred fracture path. In the beginning (Fig. 7a), however, mode-I fracture propagation away from the pre-existing fracture (negative y-direction) is still less expensive than turning mixed-mode fracture growth (also remember that the stress in y-direction is higher than the x-direction). Thus, the hydraulic

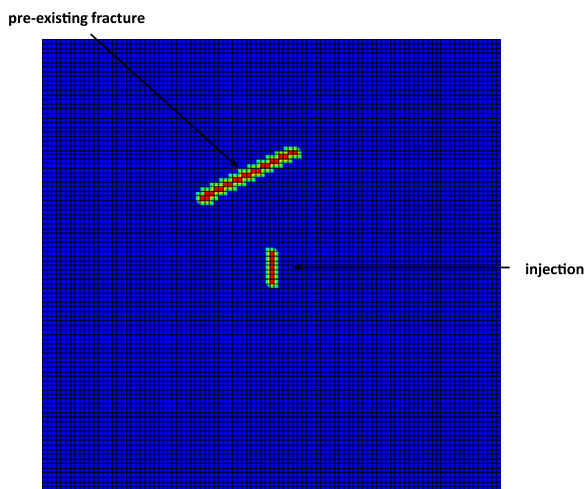


Fig. 5. An example with a pre-existing fracture in 2D.

fracture propagates in mode-I in the negative y-direction until the turning mix-mode fracture energy becomes less costly. The angle of the turning fracture constantly changes as it seeks less expensive propagation paths in the competition between the stretches imposed by the pre-existing fracture and the mixed-mode propagation (Fig. 7c). The angle becomes parallel to y-direction again by the time the hydraulic fracture grows around the stretched region and propagates further towards the upper boundary (positive y-direction) as can be seen in Fig. 7d. Discerning eyes may have caught a small kink in the almost straight hydraulic fracture propagation in the lower y-direction. It is caused by the compressed formation induced by the turning part of the fracture above and is nudged away a little bit in negative x direction. It should be emphasized that the fracture had to turn its propagating direction continuously seeking for optimal paths throughout the simulation.

The pressure profiles at each stage of fracture propagations in Fig. 7 are shown in Fig. 8. The pore-pressure profiles show that the fluid follows the fracture propagation path and more fluid leak-off (higher pressure) closer to the injection source. Also, the pressure is the highest at the injection source and gradually decreases toward the fracture tips. Thus, the fracture propagation is not only influenced by the geometric factors but also by the pressure gradient within the fracture. This phenomenon is especially noticeable in Fig. 8c as the pressure at the upper fracture tip (turning part) is clearly lower than the pressure at the lower fracture tip. This corresponds to the time the hydraulic fracture starts propagating both upwards and downwards, which indicates different fracture propagation pressures at each tip of the fracture.

The exact same simulation was carried out with the unilateral contact condition. Fig. 9 shows the displacement fields at the initial state. As the unilateral contact condition does not allow interpenetration of fracture, the impact of the natural fracture onto the initial displacement fields is nearly negligible. Only small disturbances in the vicinity due to the shear slippage on the pre-existing fracture can be observed. Fig. 10 and Fig. 11 show propagation of fracture and evolution of the pore-pressures as the water is injected. Unlike the previous example without the unilateral contact condition, the propagation direction is not deviated by the presence of the existing fracture since no interpenetration is allowed. The fracture propagates along the initial geometry which is aligned with the maximum stress direction (Fig. 10a). It grows straight into the existing fracture (Fig. 10b) and merges (Fig. 10c). The pressure profile evolution simply follows the fracture until the merger with the pre-existing fracture. Since the permeability in the pre-existing fracture is high, the hydraulic fracture experiences sudden drop in the pressure when it hits the pre-existing fracture. The pressure needs to recover to promote further propagation and fracture propagation is stalled in the meantime. When the pressure reaches to a propagation pressure, the fracture propagation resumes towards the bottom of the domain (negative y-direction) while the pressure in the existing fracture builds up (Fig. 11c). Once the pressure in the existing fracture reaches to a critical point (Fig. 11d), propagation from the existing fracture takes off, however, from a different point from the merging point or the fracture tips (Fig. 10d). In this case, the optimal path was chosen to be somewhere between the merging point and the fracture tip given the geometry, the in-situ stresses, the pore-pressure, and the boundary effect.<sup>c</sup> Comparing Fig. 7d to Fig. 10d, the impact of the unilateral contact condition is obvious in the presence of pre-existing fracture(s).

<sup>c</sup> In order to investigate detailed hydraulic fracture crossing mechanisms, specially designed studies in a more controlled setting (e.g. far boundaries) would be necessary. Interested readers on this subject are referred to Gu et al.<sup>8</sup> for example.

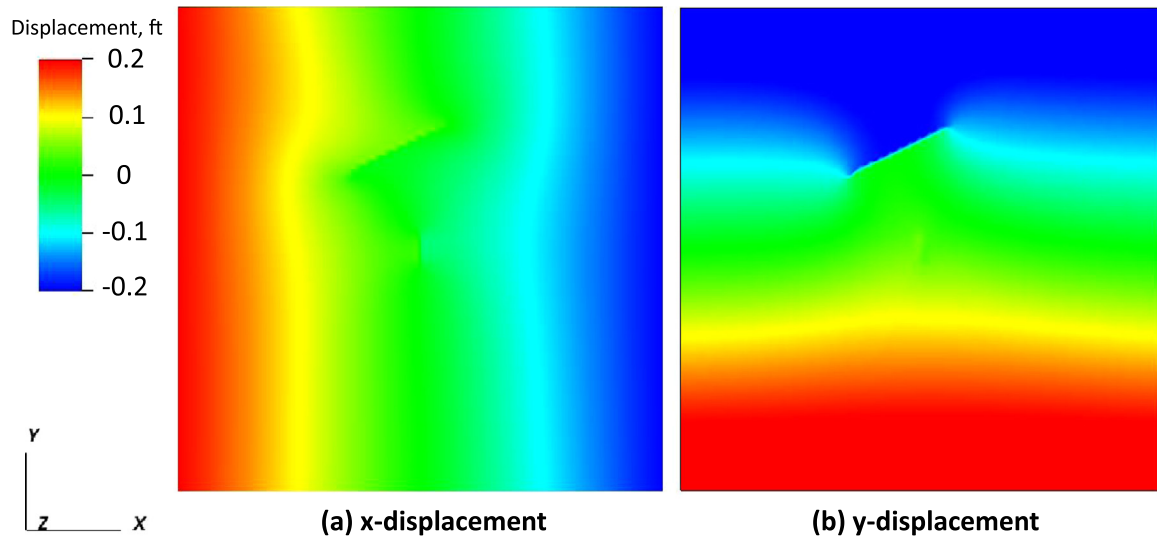


Fig. 6. The initial displacement fields with a pre-existing fracture without unilateral contact, (a) in x-direction and (b) y-direction.

4.2. 3D example

2D simulation of hydraulic fracturing is often preferred because of its ease of model/mesh preparation and less computational expense. However, the main assumption for 2D fracture is plane strain (also

known as KGD fracture) and is a reasonable assumption only in special circumstances in a flat layer system where a short and wide vertical fracture propagates throughout the layer.<sup>47</sup> In this example, we repeat a similar experiment to the previous 2D examples and investigate the “3D effects” on hydraulic fracture propagation with pre-existing fractures.

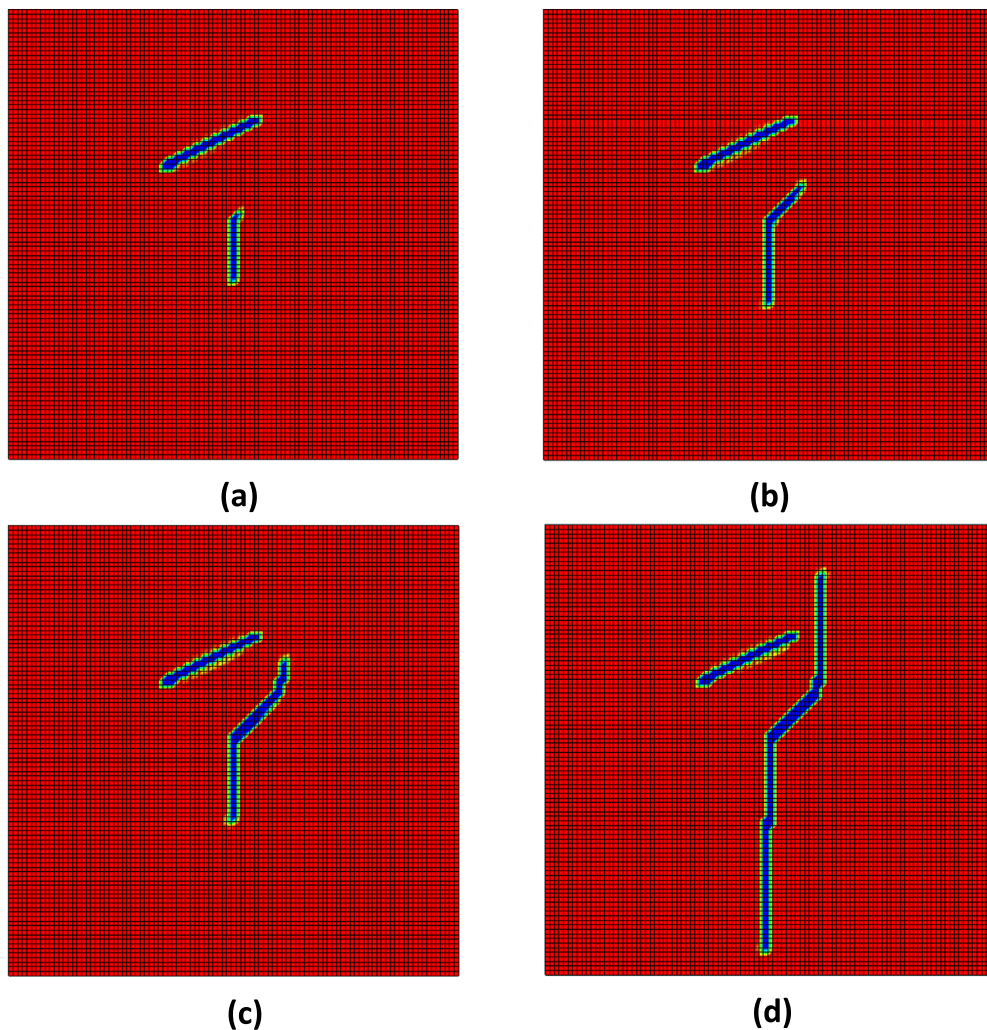


Fig. 7. Fracture propagation with the pre-existing fracture at injection volume of: (a) 0.54 bbl, (b) 0.86 bbl, (c) 1.13 bbl, and (d) 3.54 bbl.

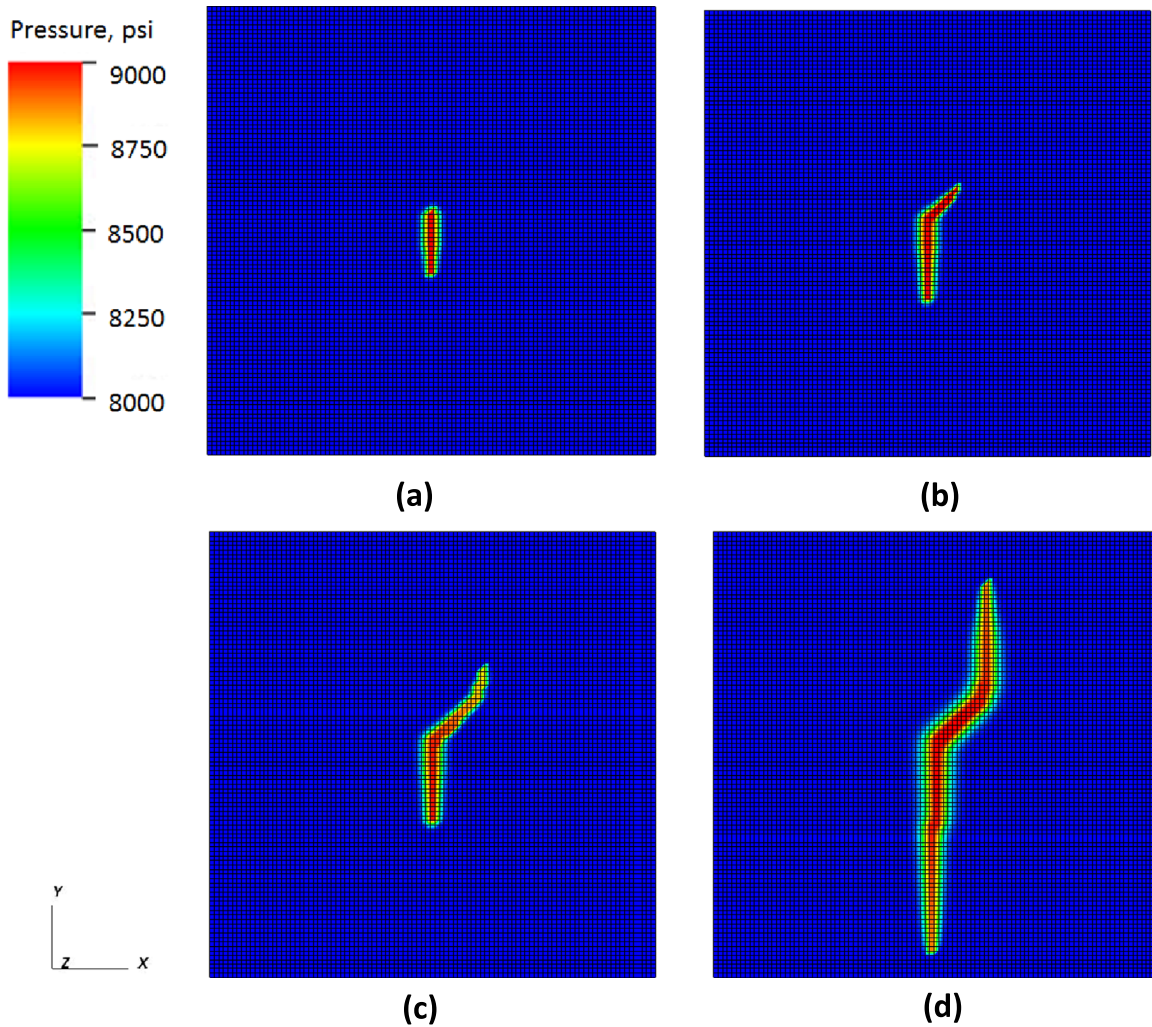


Fig. 8. Pore-pressure evolution with the pre-existing fracture at injection volume of: (a) 0.54 bbl, (b) 0.86 bbl, (c) 1.13 bbl, and (d) 3.54 bbl.

All the properties considered in 3D examples are identical to the examples in the code testing. For in-situ stresses, 8700 psi, 8500 psi, and 8700 psi are considered in x, y, and z direction respectively, and the computation axis is aligned with principle stress direction. Fig. 12 shows initial fractures in this 3D example.

An oblique penny-shaped fracture with 80 ft radius, and the strike and dip is 90° and 60° from y-axis and z-axis respectively, is located 160 ft above the hydraulic fracture with radius of 20 ft where injection takes place. Again in this example, a regular structured mesh is used and the oblique fracture, which does not conform the

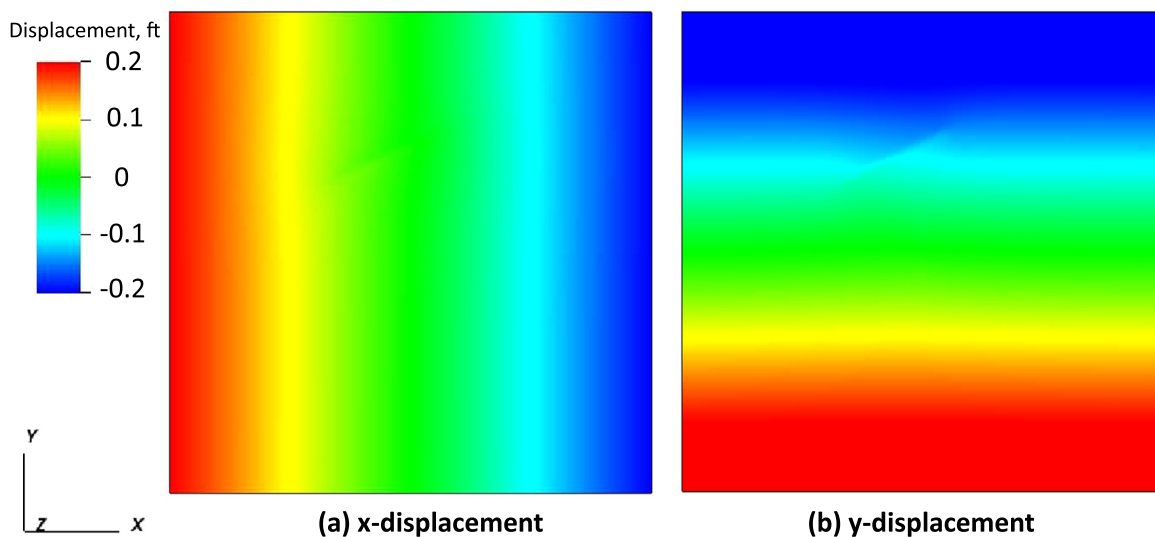
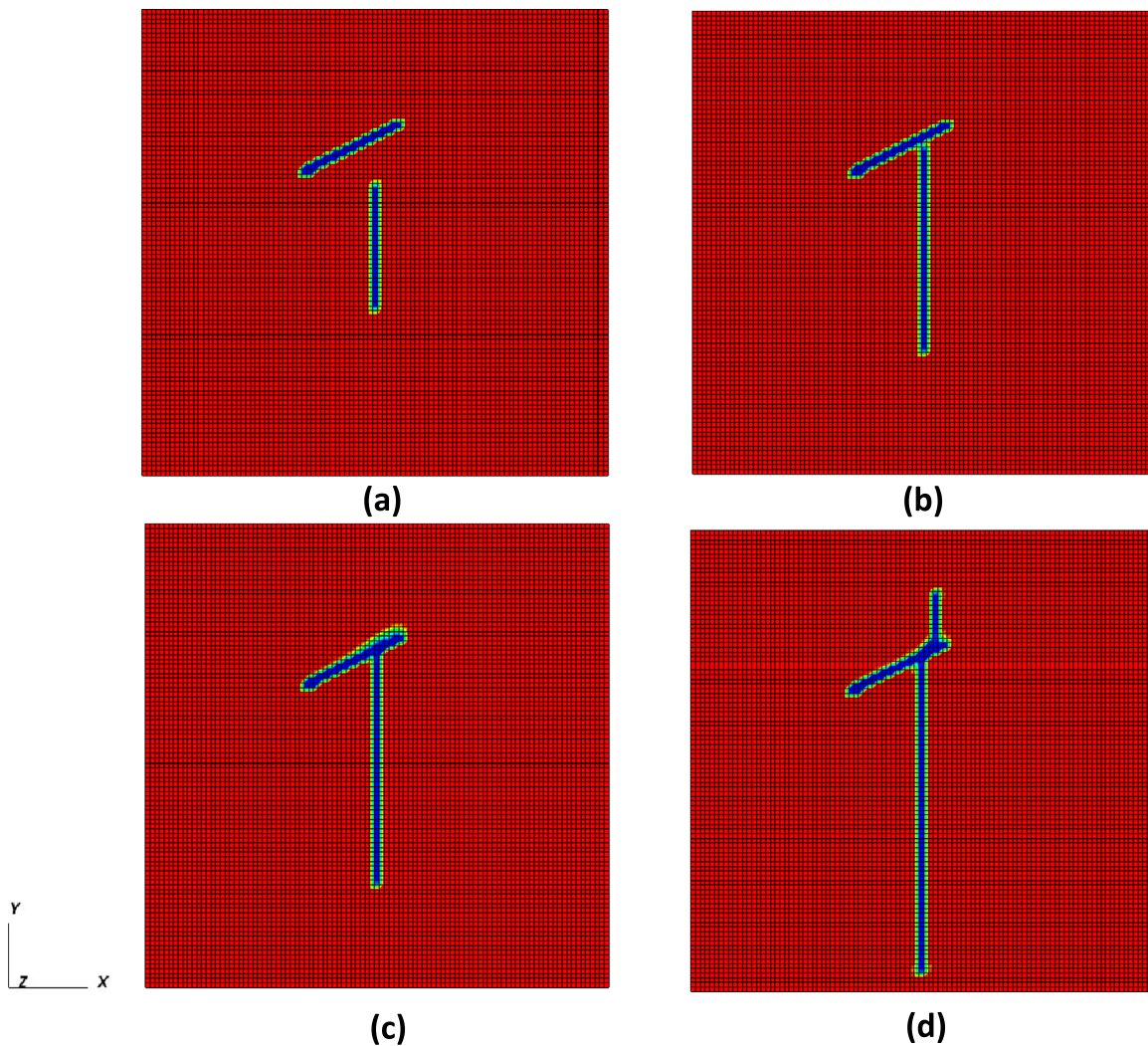


Fig. 9. The initial displacement fields with a pre-existing fracture with the unilateral contact condition, (a) in x-direction and (b) in y-direction.



**Fig. 10.** Fracture propagation with the pre-existing fracture with the unilateral contact condition at injection volume of: (a) 0.86 bbl, (b) 1.46 bbl, (c) 2.71 bbl, and (d) 4.19 bbl.

mesh, is represented using the phase-field variable. Fig. 13 shows evolution of the fractures with the injection.

The observed fracture behavior in 3D is very similar at least in the beginning to the 2D case where a plane strain condition is assumed. It grows and merges with the pre-existing fracture. The hydraulic fracture growth does not exhibit exacerbated asymmetry until it hits the pre-existing fracture (Fig. 13a). Once the fractures merge, the hydraulic fracture growth is hampered in the direction bypassing the pre-existing fracture, and the hydraulic fracture grows in the other directions on x-z plane (negative z-direction), orthogonal to the minimum stress (Fig. 13b). These observations are very similar to the 2D example. However, instead of crossing the pre-existing fracture, the hydraulic fracture grows further in x-direction without crossing the pre-existing fracture (Fig. 13c). We can see that the pre-existing fracture almost behaves as a barrier for the hydraulic fracture further growth. Despite the blockage by the pre-existing fracture, two growing fracture fronts eventually merge and create a connected fracture plane with a small curvature right above the pre-existing fracture (Fig. 13d). If we were to look at only the final fracture geometry, it would seem as if the hydraulic fracture crossed the pre-existing fracture, but the actual process to arrive at this result depicts a very different story. This result indicates the need to monitor real-time fracture growth in experiments to study fracture interaction. Note that the volume of injection to achieve this fracture propagation resulted in unrealistic amount for hydraulic fracturing process. This is partly

due to the large leak off volume and the low viscosity of water in order to achieve the required pressures for fracture propagation.

As a last example, we will demonstrate the model's capability of handling multiple fractures without the need to implement further fracture propagation criteria or special computational elements. Fig. 14 shows an initial setting of the computation. Similarly to the last 3D example, water is injected through a small initial fracture in the middle. In addition to the fracture above the injection point, three more fractures are considered with the strike and dip of 120° and 70° (below), 110° and 20° (near x), and 150° and 40° (far x) respectively, and all are distanced by 160 ft from the injection point (measured from the center of the disk to the center). All other properties including the in-situ stresses are the same as the previous example. Evolution of the fractures painted with pressure is shown in Fig. 15. The hydraulic fracture firstly merges with a fracture located far x-direction (Fig. 15a) as the tip of this far x-direction fracture is the closest. Until it merges with the pre-existing fracture, the hydraulic fracture is "attracted" to grow towards it. However, once they merge, fracture growth in that direction is curbed and is preferred in other directions. In this case, the hydraulic fracture decides to grow downward next until it finds another pre-existing fracture (Fig. 15b). Following another merger with the pre-existing fracture in low z-direction, it starts to propagate towards the one in near x-direction (Fig. 15c). Lastly, after coalescing with the near x fracture, the hydraulic fracture propagates in the direction away from all the merged fractures,

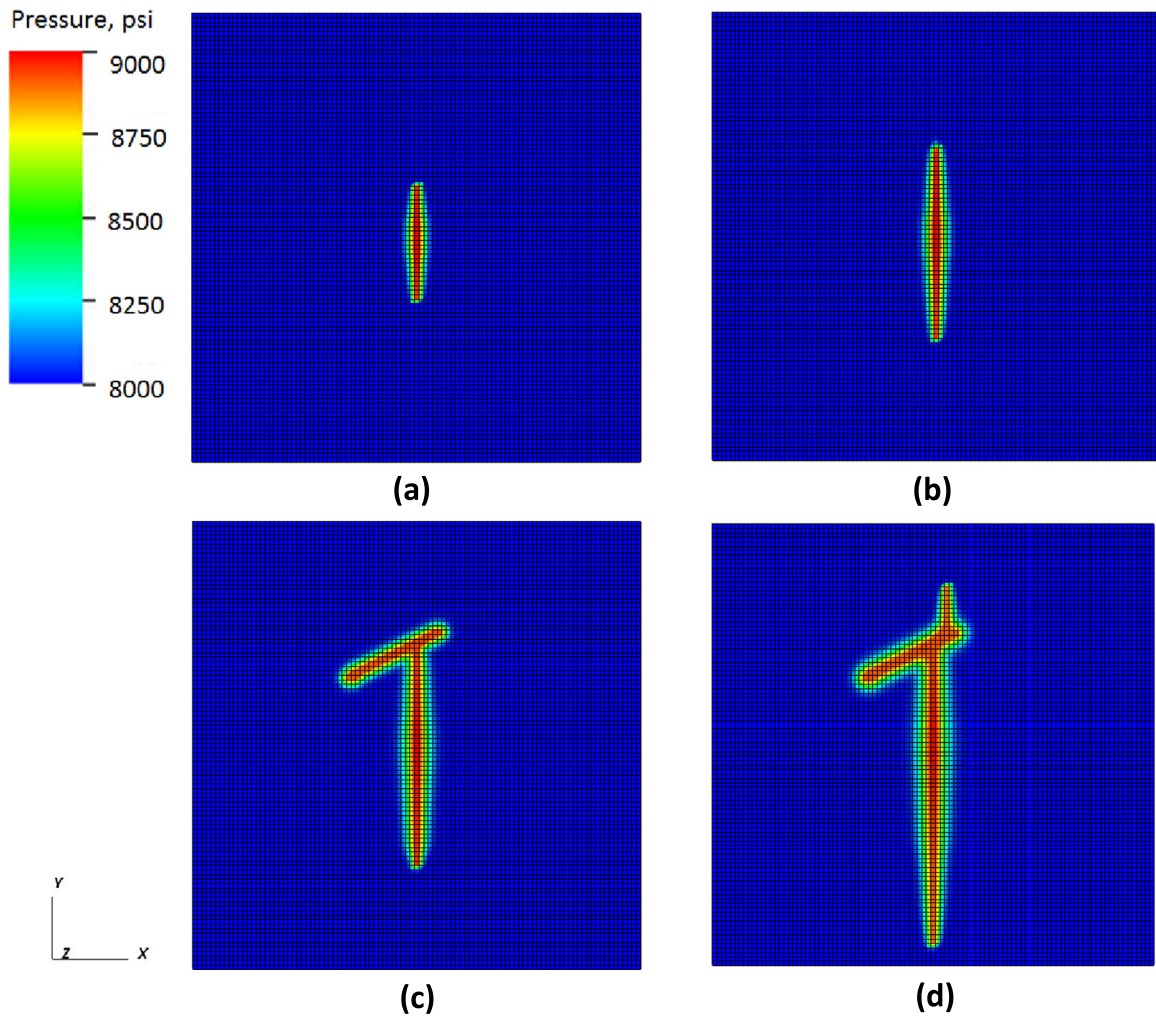


**Fig. 11.** Pore-pressure evolution with the pre-existing fracture with the unilateral contact condition at injection volume of: (a) 0.86 bbl, (b) 1.46 bbl, (c) 2.71 bbl, and (d) 4.19 bbl.

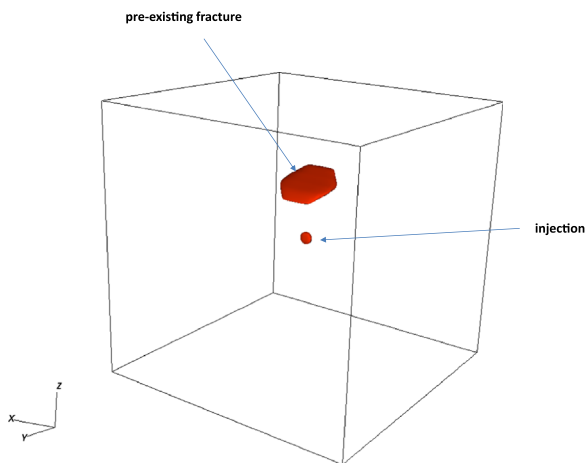


**Fig. 12.** An example with a pre-existing fracture in 3D.

which is upward. Once all the fractures are merged, its dominant propagation direction becomes the near x fracture on the same plane (Fig. 15d). The choice for this direction is favored because the near x fracture has the least dip from the plane orthogonal to the least stress and requires the least energy to propagate.

## 5. Conclusion

We have extended the phase field fracture model, which was originally developed for dry fracture, to hydraulic fracturing by including: 1) hydraulic force applied on the fracture lips, 2) poroelasticity in the regularized total energy formulation, and 3) in-situ stresses in the rock formation. The developed fracture model is iteratively coupled to an external reservoir simulator, which takes permeability multipliers from the fracture model and provides pressure field in return. We have demonstrated that a coupled model with capabilities of predicting complex fracture behaviors including turning, merging, and initiation in 3D can be built with minimum changes to an existing reservoir simulator. As commercial scale reservoir simulators keep evolving to satisfy critical requirement for specific problems (e.g. produced water, polymer or steam injection, etc.), a capability to couple to an existing reservoir simulator provides practical flexibility. However, it is not difficult to imagine that this direct iteration scheme without Jacobian matrices apparently pauses a convergence challenge. Even though some timestep will require thousands of nonlinear iterations and a small time increment for convergence, all the computations shown in the examples were carried out within a practical time<sup>d</sup> with moderate parallelization (up to 100 CPUs).

<sup>d</sup> The solution depends on not only the size of the problem but also the type.

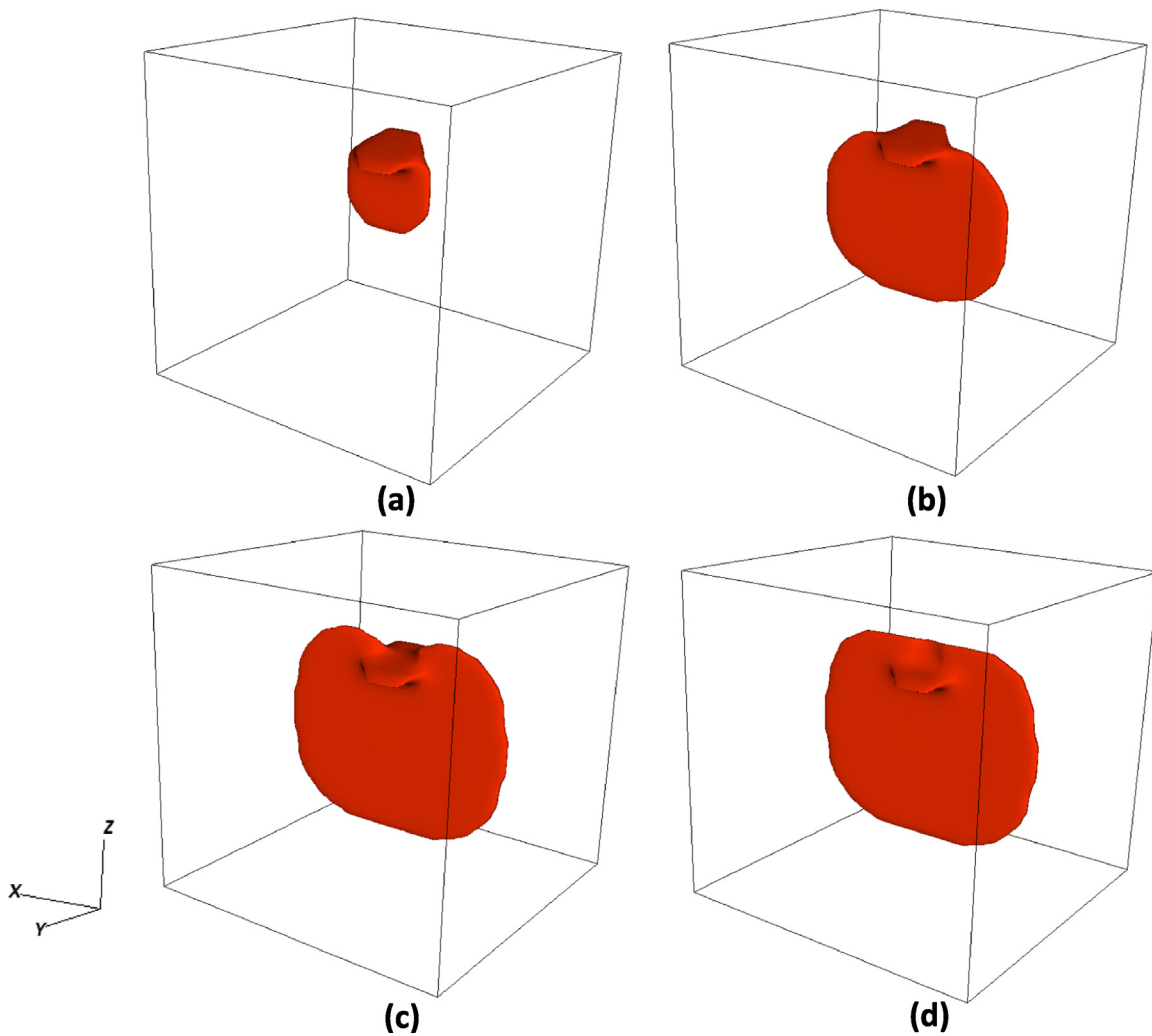


Fig. 13. Fracture propagation with the pre-existing fracture at injection volume of: (a) 1,047,308 bbl, (b) 2,766,104 bbl, (c) 3,106,301 bbl, and (d) 3,113,426 bbl.

Four random pre-existing fractures

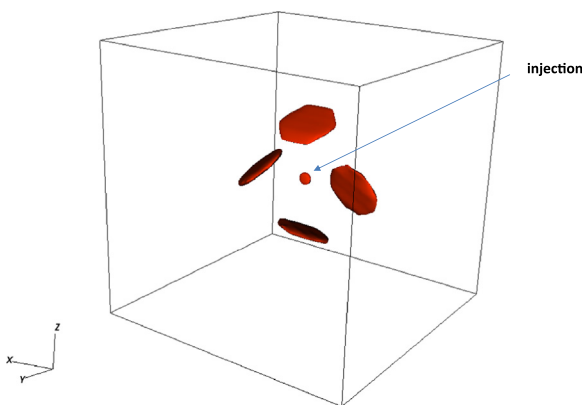


Fig. 14. An example with pre-existing fractures in 3D.

Also, our coupling is achieved through only permeability

(footnote continued)

For example, if a minimization problem is simply to solve a line crack in mode-I opening, it takes much less time than more complex minimization problem with multiple mix-mode fractures merging each other. As a general run, 2D examples were computed within hours using up to 50 CPUs and 3D examples within days (not weeks) using up to 100 CPUs.

multiplier as a function of the phase field variable that is passed to a reservoir simulator, which makes coupling with any other simulators trivial.

The proposed solution to the three-field problem was tested against the closed form solutions in 2D and 3D. Since fracture flow is not modeled using the lubrication theory, fracture behavior after the onset of fracture propagation is not compared. Despite its simplicity, fracture propagation pressures are compared reasonably with the ones obtained from a closed form solution. As for phase field fracture modeling application in hydraulic fracturing, all the published studies to date compared only static fracture opening profile,<sup>25–30</sup> and no attempts have been made to predict the critical propagation pressure or the fracture growth behavior after its onset except for the study by Bourdin et al.<sup>24</sup> done in an impermeable formation.

Furthermore, through the examples, it has been demonstrated that the variational fracture's capabilities to simulate multiple number of fractures in arbitrary paths and fracture merging, in which other approaches such as XFEM or cohesive element need yet to overcome the difficulties. For future studies in the phase field hydraulic fracture modeling, the methodology still requires a robust coupling with fluid flow through the phase field variable, an efficient and accurate formulation to estimate fracture width to be more specific. Then, the approach needs to be validated against available closed form solutions in different fracture propagation regimes (e.g. toughness, viscosity, or storage dominated)<sup>43–46</sup>

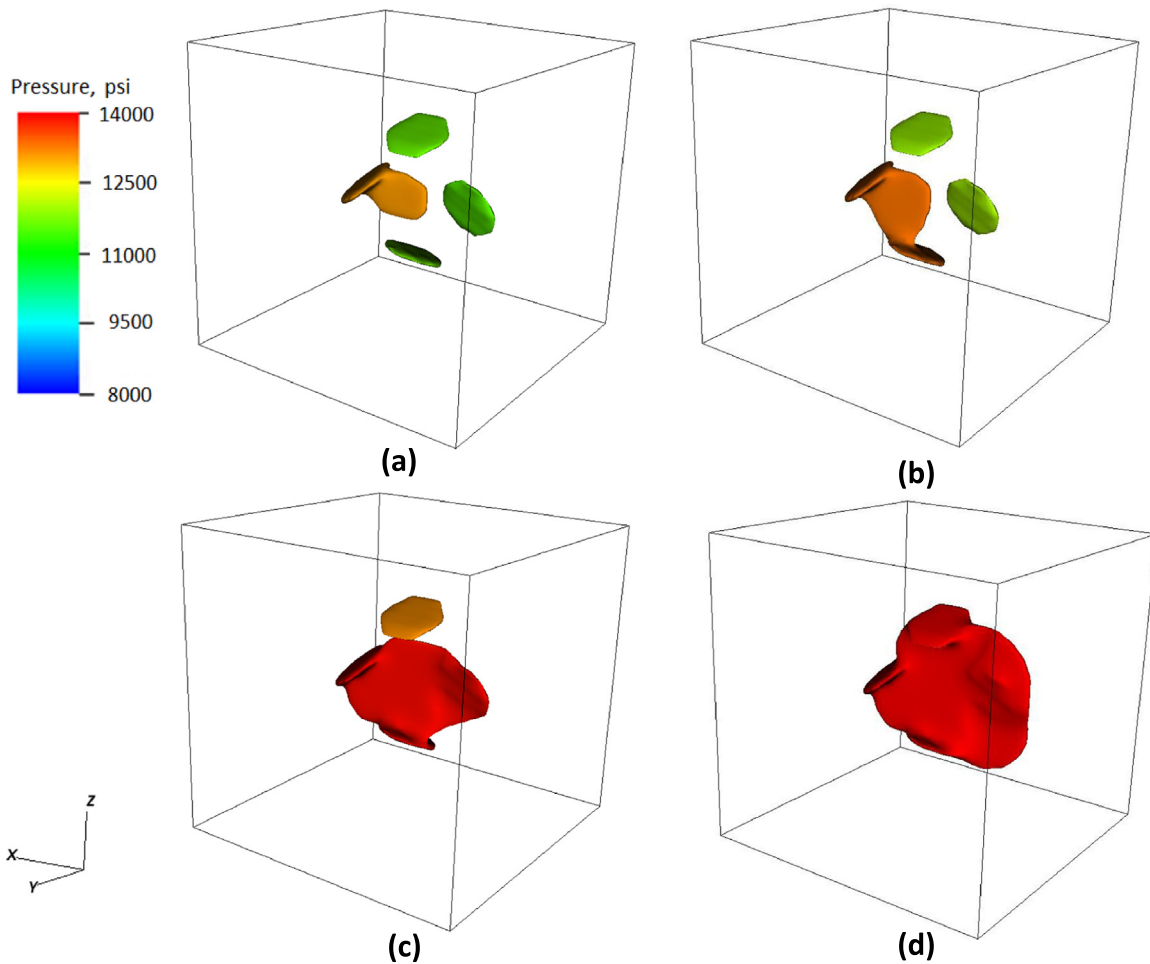


Fig. 15. Fracture propagation with the pre-existing fracture at injection volume of: (a) 94,308 bbl, (b) 3,624,679 bbl, (c) 4,522,504 bbl, and (d) 5,057,051 bbl.

especially a fluid lag (negative pressure) at the fracture tip.<sup>43</sup>

## Acknowledgments

The authors wish to thank Chevron management for permission to publish this work.

## References

- Abou-Sayed AS, Zaki KS, Wang G, Sarfare MJ, Harris MH. Produced water management strategy and water injection best practices: design, performance, and monitoring. *SPE Prod Oper.* 2007;22:59–68.
- Baker R, Dieva R, Jobling R, Lok C. The myths of waterfloods, EOR floods and how to optimize real injection schemes. In: *Proceedings of the SPE Improved Oil Recovery Conferences*. Tulsa; 11–13 April 2016.
- Roussel N, Sharma M. Optimizing fracture spacing and sequencing in horizontal-well fracturing. *SPE Prod Oper.* 2011;26:173–184.
- Peirce AP, Bungler AP. Interference fracturing: non uniform distributions of perforation clusters that promote simultaneous growth of multiple hydraulic fractures. *SPE J.* 2015;20:384–395.
- Liu C, Zhang YP, Deng D, Wu H. Optimal spacing of staged fracturing in horizontal shale-gas well. *J Pet Sci Eng.* 2015;132:86–93.
- Adachi J, Siebrits E, Peirce A, Desroches J. Computer simulation of hydraulic fractures. *Int J Rock Mech Min Sci.* 2007;44:739–757.
- Lujun J, Settari A, Sullivan RB. A novel hydraulic fracturing model fully coupled with geomechanics and reservoir simulation. *SPE J.* 2009;14:423–430.
- Dean RH, Schmidt JH. Hydraulic-Fracture predictions with a fully coupled geomechanical reservoir simulator. *SPE J.* 2009;14:707–714.
- Secchi S, Schrefler BA. A method for 3-D hydraulic fracturing simulation. *Int J Fract.* 2012;178:245–258.
- Rethore J, de Borst R, Abellan MA. A two-scale model for fluid flow in an unsaturated porous medium with cohesive cracks. *Comput Mech.* 2008;42:227–238.
- Kresse O, Weng X, Gu H, Wu R. Numerical modeling of hydraulic fracture interaction in complex naturally fractured formations. *Rock Mech Rock Eng.* 2013;46:555–568.
- McClure M, Babazadeh M, Shiozawa S, Huang J. Fully coupled hydromechanical simulation of hydraulic fracturing in three-dimensional discrete fracture networks. In: *Proceedings of the 2015 Hydraulic Fracturing Technology Conference*. the Woodlands; 3–5 February 2015.
- Gu H, Weng X. Criterion for fractures crossing frictional interfaces at non-orthogonal angles. In: *Proceedings of the 44th US Rock Mechanics Symposium*. Salt Lake City; 27–30 June 2010.
- Nagel NB, Sanchez-Nagel MA, Zhang F, Garcia X, Lee B. Coupled numerical evaluations of the geomechanical interactions between a hydraulic fracture stimulation and a natural fracture system in shale formations. *Rock Mech Rock Eng.* 2013;46:581–609.
- Wu K, Olson JE. Simultaneous multifracture treatments: fully coupled fluid flow and fracture mechanics for horizontal wells. *SPE J.* 2015;20:337–346.
- Rungamornrat J, Mear M. A weakly-singular SGBEM for analysis of cracks in 3D anisotropic media. *Comput Methods Appl Mech Eng.* 2008;197:4319–4332.
- Castonguay ST, Mear ME, Dean RH, Schmidt JH. Predictions of the growth of multiple interacting hydraulic fractures in three dimensions. In: *Proceedings of the 2013 SPE Annual Technical Conference and Exhibition*. New Orleans; 30 September–2 October 2013.
- Lecampion B. An extended finite element method for hydraulic fracture problems. *Commun Numer Methods Eng.* 2008;25:121–133.
- Dahi-Taleghani A, Olson JE. Numerical modeling of multistranded hydraulic-fracture propagation: accounting for the interaction between induced and natural fractures. *SPE J.* 2011;16:575–581.
- Gordeliy E, Peirce A. Enrichment strategies and convergence properties of the XFEM for hydraulic fracture problems. *Comput Methods Appl Mech Eng.* 2015;283:474–502.
- Francfort G, Marigo JJ. Revisiting brittle fracture as an energy minimization problem. *J Mech Phys Solids.* 1998;46:1319–1342.
- Bourdin B, Francfort GA, Marigo JJ. Numerical experiments in revisited brittle fracture. *J Mech Phys Solids.* 2000;48:797–826.
- Bourdin B, Francfort GA, Marigo JJ. The variational approach to fracture. *J Elast.* 2008;91:1–148.

24. Bourdin B, Chukwudozie CP, Yoshioka K. A variational approach to the numerical simulation of hydraulic fracturing. In: *Proceedings of the 2012 SPE Annual Technical Conference and Exhibition*, San Antonio; 8–10 October 2012.
25. Wheeler MF, Wick T, Wollner W. An augmented-lagrangian method for the phase-field approaches for pressurized fractures. *Comput Methods Appl Mech Eng*. 2008;197:4319–4332.
26. Mikelic A, Wheeler MF, Wick T. Phase-field modeling of a fluid-driven fracture in a poroelastic medium. *Comput Geosci*. 2015;19:1171–1195.
27. Heister T, Wheeler MF, Wick T. A primal-dual active set method and predictor-corrector mesh adaptivity for computing fracture propagation using a phase-field approach. *Comput Methods Appl Mech Eng*. 2015;290:466–495.
28. Miehe C, Mauthe S, Teichtmeister S. Minimization principles for the coupled problem of Darcy-Biot-type fluid transport in porous media linked to phase field modeling of fracture. *J Mech Phys Solids*. 2015;82:186–217.
29. Lee S, Wheeler MF, Wick T. Pressure and fluid-driven fracture propagation in porous media using an adaptive finite element phase field model. *Comput Methods Appl Mech Eng*. 2016;305:111–132.
30. Wick T, Singh G, Wheeler MF. Fluid-filled fracture propagation with a phase-field approach and coupling to a reservoir simulator. *SPE J*. 2015;21:981–999.
31. Miehe C, Welshinger F, Hofacker M. Thermodynamically consistent phase-field models of fracture: variational principles and multi-field FE implementations. *Int J Numer Meth Eng*. 2010;83:1273–1311.
32. Chukwudozie CP. *Application of the Variational Fracture Model to Hydraulic Fracturing in Poroelastic Media [PhD Thesis]*. Baton Rouge: Louisiana State University; 2016.
33. Wilson ZA, Landis CM. *Phase-Field Modeling of Hydraulic Fracture. ICES Report*. The University of Texas at Austin; 2016.
34. Ambrosio L, Tortorelli VM. Approximation of functionals depending on jumps by elliptic functionals via gamma-convergence. *Commun Pure Appl Math*. 1990;43:999–1036.
35. Ambrosio L, Tortorelli VM. On the approximation of free discontinuity problems. *Boll Un Mat Ital*. 1992;6:105–123.
36. Freddi F, Royer-Carfagni G. Regularized variational theories of fracture: a unified approach. *J Mech Phys Solids*. 2010;58:1154–1174.
37. Li T, Marigo JJ, Guilbaud D, Potapov S. Gradient damage modeling of brittle fracture in an explicit dynamics context. *Int J Numer Methods Eng*. 2016.
38. Amor H, Marigo JJ, Maurini C. Regularized formulation of the variational brittle fracture with unilateral contact: numerical experiments. *J Mech Phys Solids*. 2009;57:1209–1229.
39. Balay S, Abhyankar S, Adams MF, et al. *PETSc Users Manual*. Argonne National Laboratory; 2015.
40. Balay S, Abhyankar S, Adams MF, Brown J, Brune P, Buschelman K, Dalcin L, Eijkhout V, Gropp WD, Kaushik D, Knepley MG, McInnes LC, Rupp K, Smith BF, Zampini S, Zhang H. PETSc Web page. Argonne National Laboratory; 2015. (Available): (<http://www.mcs.anl.gov/petsc>).
41. Sneddon IN, Lowengrub M. *Crack Problems in the Classical Theory of Elasticity*. New York City, New York: John Wiley & Sons; 1969.
42. Abe H, Keer L, Mura T. Growth rate of a penny-shaped crack in hydraulic fracturing of rocks. *J Geophys Res*. 1976;81:5335–5340.
43. Garagash G, Detournay E. The tip region of a fluid-driven fracture in an elastic medium. *J Appl Mech*. 2000;67:183–192.
44. Savitski A, Detournay E. Propagation of a fluid-driven penny-shaped fracture in an impermeable rock: asymptotic solutions. *Int J Solids Struct*. 2002;26:6311–6337.
45. Bungier A, Detournay E, Garagash D. Toughness-dominated hydraulic fracture with leak-off. *Int J Fract*. 2005;134:175–190.
46. Adachi J, Detournay E. Self-similar solution of a plane-strain fracture driven by a power-law fluid. *Int J Numer Anal Met Geomech*. 2002;26:579–604.
47. Gu H, Weng X, Lund JB, Mack MG, Ganguly U, Suarez-Rivera R. Hydraulic fracture crossing natural fracture at nonorthogonal angles: a criterion and its validation. *SPE Prod Oper*. 2012;27:20–26.